STUDY ON SINGLE-PHASE AND TWO-PHASE FLOW AND HEAT TRANSFER CHARACTERISTICS OF HFE-7100 IN MANIFOLD MICRO-CHANNEL HEAT SINK WITH CORRUGATED BOTTOM

by

Jianping CHENG[a], Hongsen XU[a], Zhiguo TANG[a]*, and Pei ZHOU[b]

[a]School of Mechanical Engineering, Hefei University of Technology, Hefei, China
[b]School of Automotive and Transportation Engineering, Hefei University of Technology, Hefei, China

To solve the problem of high heat flux heat dissipation in microelectronic devices, a manifold micro-channel heat sink with corrugated bottom (CB-MMC) is proposed on the basis of the manifold microchannel heat sink (MMC). The flow and heat transfer characteristics of HFE-7100 in MMC and CB-MMC are investigated numerically. The results show that CB-MMC reduces the pressure loss and enhances the heat transfer performance in single-phase flow. The orthogonal test method is used to obtain structural design solutions with optimal thermal performance. It is observed that the temperature reduction is always at the expense of the increase of the pressure drop. In addition, the optimization parameters combination obtained through comprehensive evaluation of temperature and pressure drop through weight matrix – optimized solution 19 (wavelength A = 800 μm, amplitude B = 40 μm, channel depth C = 180 μm, outlet width D = 300 μm, channel width E = 25 μm). Its T_{ave} has decreased by 6.89 °C, ΔP decreased by 10.27 kPa. Moreover, the subcooled boiling flow and heat transfer performance in MMC and CB-MMC are comparatively studied. The results demonstrate that the dynamic behavior of vapor bubbles causes large pressure fluctuations, which further leads to small temperature fluctuations, and thus reduces the stability of the flow and boiling heat transfer. Compared with MMC, CB-MMC exhibits more stable two-phase flow and better boiling heat transfer.
Key words: MMC, corrugated bottom, orthogonal test, flow boiling, enhanced heat transfer

Introduction

With the development of the electronic technology, highly integrated and miniaturized electronic devices have been widely used, which led to the increasing heat flux of electronic devices. Some high-power electronic devices dissipate heat flux greater than 1000 W/cm^2 [1], and thus they work at higher temperature, which leads to thermal failure. Therefore, it is critical to select a suitable heat dissipation technology for high heat flux microelectronic devices. In Tuckerman and Pease [2] first proposed a micro-channel liquid cooling method, which integrates micro-channels on the back side of the electronic chip and uses water as coolant for

1820

Cheng, J., *et al.*: Study on Single-Phase and Two-Phase Flow and …
THERMAL SCIENCE: Year 2024, Vol. 28, No. 2C, pp. 1819-1836

forced convection heat transfer. Their experiment proved the high efficiency heat transfer capability of the microchannel heat sink (TMC). Many studies on this technology were then conducted [3, 4].

The studies on TMC mainly focused on the design of sectional shapes [5-7], geometric parameters [8-10], and disturbance structures in the microchannel [11]. In the study of microchannel sectional shapes, it is considered that the rectangular section has smaller flow resistance [7] and higher heat transfer performance than the trapezoidal and triangular sections [6]. In the study of the geometrical parameters of rectangular micro-channels, the ratio of depth to width [8] and the hydraulic diameter [10] of these micro-channels are the main factors affecting the friction coefficient and Nusselt number. To obtain higher flow and heat transfer performance, many researchers designed different disturbance structures within the micro-channels, including ribs [12], fins [13], and corrugated structures [14]. For instance, Wan *et al.* [14] introduced the semi-corrugated structure into the micro-channel, which resulted in lower flow resistance and thermal resistance.

However, Kermani *et al.* [15] found two main disadvantages of the conventional TMC: the high pressure drop and large temperature difference due to the long channels. Therefore, Harpole and Eninger [16] proposed the MMC heat sink, which adds a distributor structure to the TMC. The new design was found to significantly reduce the pressure drop and temperature difference due to the shortened flow path of the coolant. Many studies on MMC were then conducted, while mainly focus on the design of inlet and outlet flow channels [17-19], geometric parameters of MMC [20, 21], and channel bottom structure [22]. In order to optimize the manifold inlet and outlet channels, Tang *et al.* [18] changed the intake manifold channel and the intake plenum chamber into a conical contraction structure based on the self-similar heat sink, to alleviate the uneven flow distribution inside MMC. In the studies on the geometric parameters of MMC, there are mainly the inlet/outlet ratios of micro-channel [20] and aspect ratios of channel section [21]. For instance, Pourfattah *et al.* [20] numerically found that the optimal heat transfer and flow performance of MMC can be obtained at the inlet/outlet ratio of 0.25, Reynolds number of 100, and nanoparticle volume fraction of 2%. Pan *et al.* [21] demonstrated that there is an optimum aspect ratio that allows the MMC to achieve optimal heat transfer. Furthermore, they determined the functional relationship between the optimal aspect ratio and the Prandtl number, Reynolds number, and the ratio of the thermal conductivity between channel wall and coolant. In addition, many studies on adding enhanced heat transfer structures to the inner wall of MMC were conducted, including added ribs [23], fins [24, 25] and porous media [26]. For instance, Adio *et al.* [23] introduced four rib structures in MMC: forward triangular, rectangular, backward triangular, and semicircular ribs. They found that the overall heat transfer characteristics of all the sidewall ribbed MMC are higher than that of the smooth MMC, while the rectangular ribbed MMC obtained the largest performance enhancement. Pan *et al.* [25] introduced staggered pin-fin in MMC to obtain higher heat transfer performance and better temperature uniformity. Chen *et al.* [26] introduced porous fins in MMC, and showed that the MMC with 75% proportion of porous fins has the highest performance with a 19.8% reduction in thermal resistance and 46.2% increase in performance evaluation criterion (PEC).

The above studies mainly focus on the single-phase heat transfer in MMC. As we all know that the boiling heat transfer can effectively enhance the heat transfer performance [27]. Drummond *et al.* [28] manufactured and experimentally studied an embedded MMC that achieves heat flux dissipation of 1020 W/cm^2 under two-phase flow conditions using HFE-7100 as the coolant. The studies on boiling heat transfer in MMC mainly focus on the vapor bubbles dynamics [29], two-phase flow distribution and evolution [30, 31], critical heat flux (CHF) [29],

Cheng, J., *et al.*: Study on Single-Phase and Two-Phase Flow and …
THERMAL SCIENCE: Year 2024, Vol. 28, No. 2C, pp. 1819-1836

1821

and boiling heat transfer enhancement [32]. In fact, the vapor bubble growth is the basic problem in the flow boiling process. Xie *et al.* [29] deduced that the Reynolds number significantly affects the growth, distribution, and evolution of bubbles. Mukherjee and Kandlikar [30] deduced that the bubble growth rate decreases with increasing the Reynolds number, and increases with increasing the superheat temperature of coolant. Lin *et al.* [31] studied the two-phase flow distribution in MMC, and explored U-shaped and HU-shaped manifold structures with low pressure drop and low thermal resistance. Xie *et al.* [29] also studied the mechanism of CHF in MMC. They deduced that CHF usually occurs in a channel having large aspect ratio and small flow rate. They also provided suggestions for the optimization of the flow field to delay CHF. In addition, the geometric parameters of MMC significantly affect the enhanced boiling heat transfer. Luo *et al.* [32] considered that when the ratio of inlet to outlet width is between 1 and 2, the heat sink shows the minimum pressure loss.

Therefore, based on the aforementioned literature, a novel MMC heat sink with corrugated bottom (CB-MMC) is proposed in this study in order to further reduce the thermal resistance and flow resistance by introducing a corrugated structure into the channel bottom of MMC heat sink. The HFE-7100, which has low boiling point and hydrophilic properties, is used as the coolant in this study, and the flow and heat transfer characteristics in MMC and CB-MMC are numerically simulated under single-phase and two-phase subcooled boiling conditions. The CB-MMC structure with the best flow and heat transfer characteristics is determined using the orthogonal test method. Finally, the two-phase flow and boiling heat transfer characteristics of MMC and CB-MMC are compared.

Physical models and numerical methods

Geometric model

Figure 1(a) shows the structure diagram of MMC. Due to the advantages of the corrugated structure in terms of reduced flow resistance and enhanced heat transfer performance [33], a novel CB-MMC is proposed by applying corrugated structure to the channel bottom of the MMC, as shown in fig. 1(b). The coolant enters the micro-channel from the manifold inlet, and it is divided into two branches in the micro-channel for fluid-solid coupled heat transfer. Finally, the coolant converges with the fluid entering from the adjacent manifold inlet and flows out. Due to the strict geometric symmetry, the single-cell model shown in figs. 1(c) and 1(d) is used as the computational domain for simulation to reduce the computational cost. The geometric parameter values are shown in tab. 1. The heat sink structures are all made of silicon, and HFE-7100 is used as coolant. The thermophysical properties of silicon and HFE-7100 are shown in tab. 2.
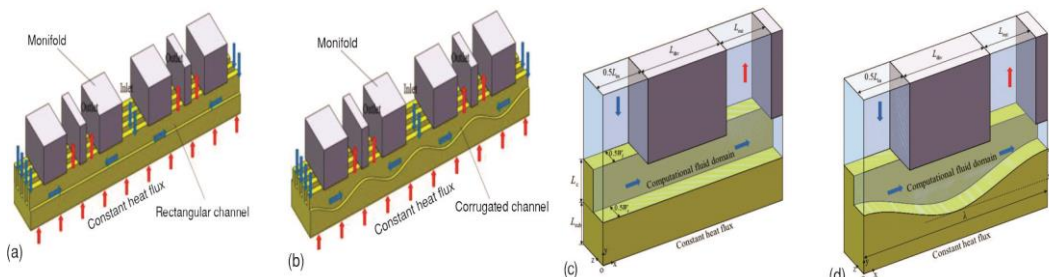
Figure 1. Geometric model; structure diagram of MMC (a) and CB-MMC (b) and computational domain of MMC (c) and CB-MMC (d)

1822

Cheng, J., *et al.*: Study on Single-Phase and Two-Phase Flow and …
THERMAL SCIENCE: Year 2024, Vol. 28, No. 2C, pp. 1819-1836

Table 1. Geometric parameter values

Parameters	Variables	Values [μm]
Length of inlet	L_{in}	400
Length of outlet	L_{out}	200
Length of divider	L_{div}	350
Heightof substrate	L_{sub}	150
Height of channel	L_c	150
Width of fin	W_f	15
Width of channel	W_c	15
Wavelength	λ	800
Amplitude	H_a	100

Table 2. Thermophysical properties of silicon and HFE-7100

	Silicon	HFE-7100 (single-phase)	HFE-7100 (liquid)	HFE-7100 (vapor)
ρ, [kgm^{-3}]	2330	1420	1402	11.5
C_p, [Jkg^{-1}K^{-1}]	712	1500	1263	870
k, [Wm^{-1}K^{-1}]	148	0.059	0.058	0.01
μ, [kgm^{-1}s^{-1}]		4.34×10^{-4}	4.00×10^{-4}	1.32×10^{-5}
i_{lv}, [kJkg^{-1}]		111.6		
σ, [Nm^{-1}]		9.43×10^{-3}		

* The saturation temperature of liquid HFE-7100 $T_{sat} = T_{ref} = 339$K

Governing equations

To correctly describe the simulation process, the following assumptions are made: the fluid is incompressible and Newtonian, the fluid and solid have constant thermophysical properties, and the viscous dissipation and contact thermal resistance are neglected.

When the single-phase heat transfer occurs in the channel, it can be treated as a fluid-solid coupled heat transfer problem, and the flow can be considered as a steady-state laminar flow [24]. Its continuity, momentum, and energy equations are given by [21]:

$$\nabla \cdot \boldsymbol{u} = 0 \tag{1}$$

$$(\boldsymbol{u} \cdot \nabla)\rho_f \boldsymbol{u} = -\nabla P + \mu \nabla^2 \boldsymbol{u} \tag{2}$$

$$\rho_f c_{p,f}(\boldsymbol{u} \cdot \nabla T) = k_f \nabla^2 T \tag{3}$$

where $\boldsymbol{u}$ denotes the velocity vector of the fluid.

Energy equation in the solid domain of heat sink:

$$k_s \nabla^2 T = 0 \tag{4}$$

In subcooled flow boiling, evaporation processes of the coolant occur in the microchannel. The volume of fluid [32] method is adopted to calculate the subcooled flow boiling in MMC. The governing equations are given by [24]:

Fluid volume fraction equation

$$\frac{\partial \dot{\alpha}}{\partial t} + \nabla \cdot (\alpha \boldsymbol{u}) = \dot{\alpha}_{lv} \tag{5}$$

Cheng, J., *et al.*: Study on Single-Phase and Two-Phase Flow and …
THERMAL SCIENCE: Year 2024, Vol. 28, No. 2C, pp. 1819-1836

1823

where α is the volume fraction of the liquid phase and $\dot{\alpha}_{lv}$ is the volume fraction source term caused by phase change.

The continuity, momentum, and energy equations are:

$$\nabla \cdot \boldsymbol{u} = \dot{v}_{lv} \tag{6}$$

$$\frac{\partial(\rho \boldsymbol{u})}{\partial t} + \nabla(\rho \boldsymbol{u}\boldsymbol{u}) = \boldsymbol{f}_\sigma - \nabla p + \nabla \left[\mu \left(\nabla \boldsymbol{u} + \nabla \boldsymbol{u}^T \right) \right] \tag{7}$$

$$\frac{\partial(\rho i)}{\partial t} + \nabla(\rho \boldsymbol{u}i) = \nabla(k\nabla T) - \dot{q}_{lv} \tag{8}$$

Energy equation of the heat sink solid domain:

$$\frac{\partial(\rho c_{p,s})}{\partial t} = k_s \nabla^2 T \tag{9}$$

where

$$\boldsymbol{f}_\sigma = \sigma \kappa \boldsymbol{n} |\nabla \alpha| \frac{2\rho}{\rho_v + \rho_l} \tag{10}$$

$$\kappa = -(\nabla \cdot \boldsymbol{n}) \tag{11}$$

$$\boldsymbol{n} = \frac{\nabla \alpha}{|\nabla \alpha|} \tag{12}$$

where $\boldsymbol{f}_\sigma$ is the surface tension, σ – the surface tension coefficient, κ is defined according to the dispersion of the unit normal, and $\boldsymbol{n}$ – the unit normal.

The enthalpy value i of intermediate state is calculated by mass-averaged:

$$i = \frac{(1-\alpha)\rho_v c_{p,v} + \alpha \rho_l c_{p,l}}{\rho} \left(T - T_{ref} \right) \tag{13}$$

The density, viscosity, and thermal conductivity in the equations are calculated by volume fraction weighted average:

$$\rho = (1-\alpha)\rho_v + \alpha \rho_l \tag{14}$$

$$\mu = (1-\alpha)\mu_v + \alpha \mu_l \tag{15}$$

$$k = (1-\alpha)k_v + \alpha k_l \tag{16}$$

The empirical rate parameter model is used in this study to describe the phase change process, which is based on the Lee model [34] proposed by Yang *et al*. [35]. This model does not require to artificially set nucleation points. The mass transfer process is driven by the difference between the local and saturation temperatures. Thus the mass transfer equation is as:

$$\dot{m}_{lv} = \begin{cases} \gamma_l \alpha \rho_l \dfrac{T - T_{sat}}{T_{sat}} & \text{if } \quad T \geq T_{sat} \\[3mm] \gamma_v (1-\alpha)\rho_v \dfrac{T - T_{sat}}{T_{sat}} & \text{if } \quad T \leq T_{sat} \end{cases} \tag{17}$$

The evaporation and condensation empirical rate coefficients (γ_l and γ_v) highly depend on the simulated operating conditions, flowing geometry, and grid size. The γ should have a compromise value to ensure that the vapor-liquid interface temperature is near the saturation temperature [36]. Therefore, based on the research results of Luo *et al.* [32], it is assumed that $\gamma_l = \gamma_v = 100$.

The source term in the energy equation is determined by eqs. (13) and (17):

$$\dot{q}_{lv} = \dot{m}_{lv}\, i_{lv} \tag{18}$$

Thus, the volume evaporation rate and the phase fraction source term can be expressed:

$$\dot{v}_{lv} = \frac{\dot{q}_{lv}}{i_{lv}}\left(\frac{1}{\rho_v} - \frac{1}{\rho_l}\right) \tag{19}$$

$$\dot{\alpha}_{lv} = -\frac{\dot{q}_{lv}}{\rho i_{lv}} \tag{20}$$

Boundary conditions

In this study, the coolant enters the manifold at a constant velocity and temperature. An atmospheric pressure is specified at the manifold outlet. The bottom heat source surface is defined with a constant heat flux. Because it is far away from the heat source surface, the adiabatic boundary condition is applied to the upper solid surface. The non-slip boundary condition is applied to all fluid-solid coupled surfaces. Due to the geometrical and flow periodicity, the four sidewall surfaces of the calculation model are given symmetric boundary conditions, and the symmetry plane is set as zero gradient:

$$\frac{\partial u}{\partial n} = 0 \tag{21}$$

The coolant enters the heat sink at a constant velocity perpendicular to the inlet section, and its flow rate is computed as:

$$u = \frac{G_{in}}{\rho_l} \tag{22}$$

The fluid-solid coupled surface is continuously coupled by temperature and heat flux:

$$T_s = T_f \tag{23}$$

$$k_f \frac{\partial T_f}{\partial n} = k_s \frac{\partial T_s}{\partial n} \tag{24}$$

In the numerical calculation, the second-order upwind formats are used to discretize momentum and energy. The velocity-pressure coupling is solved using the SIMPLE algorithm, with a time step of 10^{-6} seconds. Commercial ANSYS FLUENT software is used to solve three-dimensional heat transfer and flow equations.

Verification of grid independence

Since the computational domain of CB-MMC is a rectangular structure, the structured mesh division of 3-D model can improve the computational speed and save computational resources. Figure 2 shows the hexahedral mesh of the CB-MMC computational domain and the local mesh refinement.
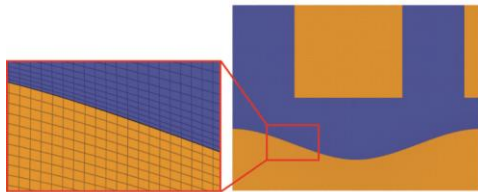
Figure 2. The CB-MMC computational domain mesh
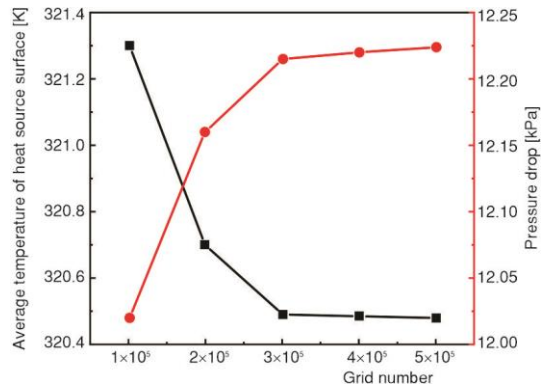
Figure 3. The impact of the grid numbers on the calculation results

The impact of the grid numbers is explored in this section. Five sets of grids with different grid numbers are considered. The number of grids ranging between 100000 and 500000. Simulations are performed for each of the five sets of grids with a microchannel flow rate of 1300 kg/m^2s and a heat flux at the bottom heat source surface of 200 W/cm^2. Figure 3 shows the impact of the grid numbers on the average temperature and the pressure drop of the CB-MMC. It is found that the trend of the average temperature and the pressure drop tends to stabilize as the grid numbers increase. The errors of the relative changes of the average temperature and the pressure drop in CB-MMC become less than 1% as the grid numbers increase from 300000 to 400000. Therefore, considering the efficiency of numerical calculation, a grid number of 300000 is used for subsequent simulation studies of 3-D model.

Validation of the simulation model

In this section, an experimental validation of the simulation model is performed. The structure of the calculation model is similar to that of the MMC experimentally studied in [28], as shown in fig. 1(c). The geometric parameters of the calculation model are shown in tab. 1. The HFE-7100 is used as the coolant. The inlet temperature is 332.15 K, and the channel mass flow rate is 1300 kg/m^2s. The heat flux in the range of 0-400 W/cm^2 is set on the bottom of CB-MMC.

Figure 4 shows the comparison between numerical simulation and experimental results. It is found that when the heat flux is less than 100 W/cm^2, almost no boiling occurs. At this time, single-phase heat transfer occurs in the channel, and the simulation results are consistent with the experimental data. When the heat flux increases from 150-400 W/cm^2, flow boiling heat transfer occurs in the channel, the simulation results are slightly higher than the experimental data, and the difference between the average temperatures of the corresponding heat source surfaces is less than 3 K. Therefore, the validation results show that the simulation model is reliable.

Results and discussion

Comparison of single-phase flow and heat transfer characteristics of MMC and CB-MMC

In this section, MMC and CB-MMC, having the same inlet width, divider width, outlet width, and channel width are compared, figs. 1(c) and 1(d). The microchannel depth of MMC is consistent with the corrugated centerline depth of CB-MMC. Therefore, the two heat sinks have the same inlet velocity when the channel mass flows are equal. The specific structural

1826

Cheng, J., *et al.*: Study on Single-Phase and Two-Phase Flow and …
THERMAL SCIENCE: Year 2024, Vol. 28, No. 2C, pp. 1819-1836

dimensions are shown in tab. 1. The bottom heat source surface of MMC and CB-MMC adopts a constant heat flux of 200 W/cm^2.

Figure 5 shows the pressure nephogram, streamline, and temperature nephogram in the MMC and CB-MMC channels for a mass flow rate of 1500 kg/m^{2}s in the single-phase flow. It can be seen from fig. 5(a) that in MMC, when the coolant flows into the micro-channel through the manifold channel, the flow rate at the inlet increases and the pressure sharply decreases due to the sudden contraction of the section and the change of the flow direction. In CB-MMC, the corrugated bottom connects the inlet and outlet channels of the manifold into a similar U-shaped structure, which reduces the flow resistance when the coolant turns. It can be observed from fig. 5(b) that the temperature distributions of MMC and CB-MMC are non-uniform, with a higher temperature of heat source surface near the manifold outlet. This is because the coolant collides with the incoming coolant from the adjacent inlet manifold at the outlet manifold where it accumulates, so that the heat cannot be discharged in time,

Figure 4. Validation of the numerical model
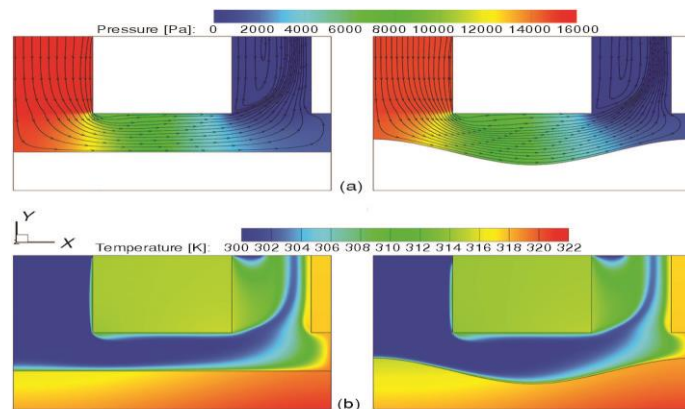
Figure 5. Comparison of pressure (a) and temperature (b) nephograms between MMC and CB-MMC

which results in increasing the temperature in this area. In addition, the maximum temperature of the heat source surface of CB-MMC is lower than that of MMC, and its temperature uniformity is also better. This is mainly because the corrugated channel has a larger heat transfer area than the rectangular channel, and therefore the temperature of CB-MMC at the inlet is lower. In addition, the coolant impinges on the corrugated surface at the outlet, which destroys the thermal boundary layer, and thus enhances the convective heat transfer at the outlet.

Figure 6 shows the variation of the average temperature of heat source surface, T_{ave}, and the pressure drop between inlet and outlet, ΔP, in MMC and CB-MMC. As can be seen from fig. 6(a), all the T_{ave} values decrease as the channel mass flow rate increases. More precisely, when the flow rate increases from 1000 kg/m^{2}s to 1500 kg/m^{2}s, the T_{ave} values of MMC and CB-MMC decrease by 4.3 °C and 3.5 °C, respectively. This is mainly due to the thinning of the thermal boundary-layer caused by the coolant at high velocity. In addition, under the same conditions, CB-MMC increases the heat transfer area. Thus, it has a lower T_{ave} values than that of MMC. Figure 6(b) shows that all the ΔP values increase as the channel flow rate increases, while the ΔP of CB-MMC is always lower than that of MMC. Under the same geometric conditions, the increase in flow velocity leads to greater disturbance to the bottom layer of the laminar flow [37], and thus enhances the heat transfer while also increasing the pressure
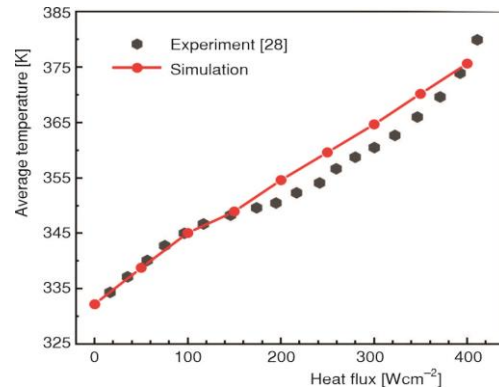
Cheng, J., *et al.*: Study on Single-Phase and Two-Phase Flow and …
THERMAL SCIENCE: Year 2024, Vol. 28, No. 2C, pp. 1819-1836

1827

loss. That is, the corrugated bottom plays a buffering role on the collision of the fluid, slows down the reduction of the flow velocity, and thus reduces the pressure loss, as shown in fig. 5. Figures 6(a) and 6(b) shows that at a channel mass flow rate of 1500 kg/m²s, the CB-MMC reduces the pressure drop by 4.1% at a temperature reduction of less than 1% compared to the MMC. It can be observed from fig. 6(c) that a greater ΔP is required for MMC to reach the same T_{ave} obtained by CB-MMC. At both T_{ave} of 48 °C, the pressure drop of the MMC increases by 9.3% compared to the CB-MMC. A lower temperature and a lower pressure drop are both often required, and thus the corresponding structure near the lower left corner of the coordinate is superior. It is deduced that the comprehensive heat transfer performance of CB-MMC is higher than that of MMC.
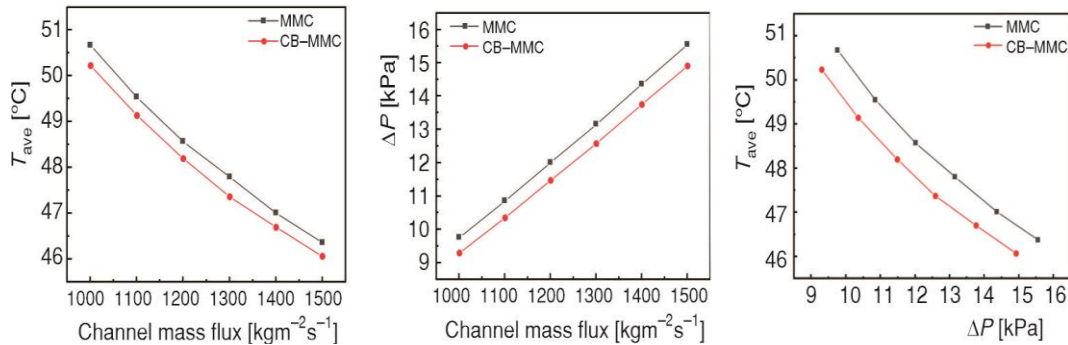

Figure 6. Comparison of T_{ave} and ΔP between MMC and CB-MMC

The orthogonal test

In this section, a multi-factor analysis of the structural parameters affecting the flow and heat transfer of the CB-MMC is performed using the orthogonal test method, so that the influence of each factor level on the test index values can be determined. Thus, the structure design of CB-MMC with the best flow and heat transfer characteristics can be determined. The core of orthogonal test is the orthogonal array which consists of various factors and their corresponding levels [38]. Therefore, the factors and levels should be first determined. The corrugated structure wavelength (A), corrugated structure amplitude (B), channel depth (C), outlet width (D), and channel width (E) are considered as the influencing factors, and T_{ave} and ΔP are used as the test indexes to establish a five-factor four-level orthogonal test, as shown in tab. 3.

Table 3. Factors and levels of the test

Levels	Factors				
	A [μm]	B [μm]	C [μm]	D [μm]	E [μm]
1	400	40	90	150	10
2	800	80	120	200	15
3	1200	120	150	250	20
4	1600	160	180	300	25

The orthogonal design table for arranging various structural factors is established according to the L_{16} (4^5) orthogonal table, as shown in tab. 4. In the table, each row represents a set of CB-MMC structural parameter combinations. The computational geometry model corresponding to each scheme in tab. 4 is then developed, and CFD simulations are performed for

1828

Cheng, J., *et al.*: Study on Single-Phase and Two-Phase Flow and …
THERMAL SCIENCE: Year 2024, Vol. 28, No. 2C, pp. 1819-1836

all the models using ANSYS Fluent. The evaluation index values obtained from the simulation are shown in tab. 4, where I and II are the evaluation indexes of T_{ave} and ΔP, respectively.

Table 4. The L_{16} (4^5) orthogonal designed table with the obtained results

Test no.	Factors					Evaluation index	
	A [μm]	B [μm]	C [μm]	D [μm]	E [μm]	I [°C]	II [kPa]
1	400	40	90	150	10	58.93	30.22
2	400	80	120	200	15	50.71	16.08
3	400	120	150	250	20	49.42	12.28
4	400	160	180	300	25	51.80	10.91
5	800	40	120	250	25	54.53	5.85
6	800	80	90	300	20	59.77	6.18
7	800	120	180	150	15	42.43	18.08
8	800	160	150	200	10	46.03	27.37
9	1200	40	150	300	15	47.01	12.53
10	1200	80	180	250	10	43.72	28.58
11	1200	120	90	200	25	59.52	7.11
12	1200	160	120	150	20	49.60	10.76
13	1600	40	180	200	20	44.53	10.93
14	1600	80	150	150	25	50.33	8.88
15	1600	120	120	300	10	54.96	26.98
16	1600	160	90	250	15	59.71	22.33

The range of the evaluation indexes is obtained based on the evaluation index values in tab. 4, as shown in tabs. 5 and 6. In these tables, K_t and k_t ($t = 1, 2, 3,$ and 4) represent the sum and the average of the evaluation index values at different levels of a factor. Therefore, $k_t = K_t/4$. The R_I and R_{II} respectively denote the ranges of the evaluation indexes I and II under a certain factor, and their values are calculated as follows: $R_{I/II} = \max(k_t) - \min(k_t)$, ($t = 1, 2, 3,$ and 4), that is, the difference between the maximum value and the minimum value of the evaluation indexes under the corresponding factor. The value reflects the range of change of the evaluation index when each factor fluctuates at different levels. The larger the value, the greater the influence of the factor on the evaluation indexes. Therefore, the order of the effects of the factors on the evaluation indexes can be determined from the range value [39].

Table 5. Range analysis of the evaluation index I

Index	Factors				
	A [μm]	B [μm]	C [μm]	D [μm]	E [μm]
K_1	210.86	205.00	237.93	201.29	203.64
K_2	202.76	204.53	209.80	200.79	199.86
K_3	199.85	206.33	192.79	207.38	203.32
K_4	209.53	207.14	182.48	213.54	216.18
k_1	52.72	51.25	59.48	50.32	50.91
k_2	50.69	**51.13**	52.45	**50.20**	**49.97**
k_3	**49.96**	51.58	48.20	51.85	50.83
k_4	52.38	51.79	**45.62**	53.39	54.05
R_I	2.76	0.66	13.86	3.19	4.08
Optimize selections	A_3	B_2	C_4	D_2	E_2

Table 6. Range analysis of the evaluation index II

Index	Factors				
	A [μm]	B [μm]	C [μm]	D [μm]	E [μm]
K_1	69.49	59.53	65.84	67.94	113.15
K_2	57.48	59.72	59.67	61.49	69.02
K_3	58.98	64.45	61.06	69.04	40.15
K_4	69.12	71.37	68.50	56.60	32.75
k_1	17.37	**14.88**	16.46	16.99	28.29
k_2	**14.37**	14.93	**14.92**	15.37	17.26
k_3	14.75	16.11	15.27	17.26	10.04
k_4	17.28	17.84	17.13	**14.15**	**8.19**
R_{II}	3.00	2.96	2.21	3.11	20.10
Optimize selections	A_2	B_1	C_2	D_4	E_4

Cheng, J., *et al.*: Study on Single-Phase and Two-Phase Flow and …
THERMAL SCIENCE: Year 2024, Vol. 28, No. 2C, pp. 1819-1836

1829

It can be deduced from tab. 5 that the primary and secondary order of the impact of each factor on evaluation index I is $C > E > D > A > B$. This indicates that factor C has the most significant effect on T_{ave}, while factor B has the least effect on it. Similarly, it can be seen from the range values in tab. 6 that the order of the influence of each factor on evaluation index II is $E > D > A > B > C$. Among the structural factors, factor E has the greatest effect on ΔP in heat sink, while factor C has the least effect on it. For evaluation indexes I and II, lower T_{ave} and ΔP are considered as more preferable selections. Therefore, the optimal solution for I obtained from tab. 5 is $A_3B_2C_4D_2E_2$ (Define it as Solution 17), and that for II obtained from tab. 6 is $A_2B_1C_2D_4E_4$ (Define it as Solution 18). The values of each structural parameter of the selected optimal solution are underlined in the table.

The previous two sets of solutions are the superior results obtained from individual evaluation indexes. To meet the requirements of two evaluation indexes at the same time, a more optimal combination solution is obtained relative to I and II. In this study, the weight matrix analysis method is used to comprehensively measure the effect weight of each factor level on two evaluation indexes, so as to rapidly determine the optimal solution. The weight matrices of the two evaluation indexes are calculated as:

- The evaluation index matrix is first established, where k_{ij} is the average of the evaluation indexes at the jth level of the ith factor. If the evaluation index is as small as possible, then K_{ij} is set to $1/k_{ij}$ and matrix, M, is constructed as:

$$
M = \begin{vmatrix}
K_{11} & 0 & 0 & \cdots & 0 \\
K_{12} & 0 & 0 & \cdots & 0 \\
\cdots & \cdots & \cdots & \cdots & \cdots \\
K_{1j} & 0 & 0 & \cdots & 0 \\
0 & K_{21} & 0 & \cdots & 0 \\
0 & K_{22} & 0 & \cdots & 0 \\
\cdots & \cdots & \cdots & \cdots & \cdots \\
0 & K_{2j} & 0 & \cdots & 0 \\
\cdots & \cdots & \cdots & \cdots & \cdots \\
0 & 0 & 0 & \cdots & K_{i1} \\
0 & 0 & 0 & \cdots & K_{i2} \\
\cdots & \cdots & \cdots & \cdots & \cdots \\
0 & 0 & 0 & \cdots & K_{ij}
\end{vmatrix}
\tag{25}
$$

By setting

$$
T_i = 1/\sum_{j=1}^{j} K_{ij}
$$

the factor matrix T is then constructed as:

$$
T = \begin{vmatrix}
T_1 & & \cdots & \\
& T_2 & \cdots & \\
\cdots & \cdots & \cdots & \cdots \\
& & \cdots & T_i
\end{vmatrix}
\tag{26}
$$

Afterwards, the level matrix is established and the range is defined as s_i. Finally, by setting:

$$S_i = s_i / \sum_{i=1}^{i} s_i$$

the S matrix is constructed as:

$$S = \begin{bmatrix} S_1 \\ S_2 \\ \dots \\ S_i \end{bmatrix} \quad (27)$$

Therefore, the weight matrix of the evaluation indexes is calculated as:
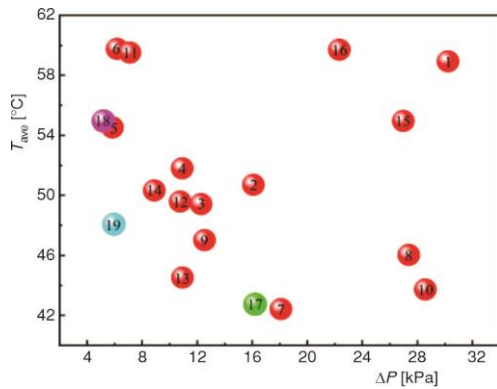
$$\omega = MTS \quad (28)$$

There are two evaluation indexes in this test. Therefore, the total weight matrix of the orthogonal test is the average of the weight matrix of the two evaluation indexes, which is calculated as:

$$\omega = \frac{\omega_{\mathrm{I}} + \omega_{\mathrm{II}}}{2} = \frac{1}{2} \left(\begin{bmatrix} 0.027409 \\ 0.028507 \\ 0.028926 \\ 0.027582 \\ 0.006744 \\ 0.006762 \\ 0.006703 \\ 0.006675 \\ 0.120818 \\ 0.137062 \\ 0.149136 \\ 0.157545 \\ 0.033182 \\ 0.033265 \\ 0.032213 \\ 0.031278 \\ 0.041943 \\ 0.042733 \\ 0.042007 \\ 0.039508 \end{bmatrix} + \begin{bmatrix} 0.021769 \\ 0.026314 \\ 0.025637 \\ 0.021882 \\ 0.025124 \\ 0.025042 \\ 0.023206 \\ 0.020956 \\ 0.017002 \\ 0.018757 \\ 0.018329 \\ 0.016339 \\ 0.023100 \\ 0.025533 \\ 0.022739 \\ 0.027739 \\ 0.071885 \\ 0.117822 \\ 0.202537 \\ 0.248291 \end{bmatrix} \right) = \begin{bmatrix} 0.02459 \\ 0.02741 \\ 0.02728 \\ 0.02473 \\ 0.01593 \\ 0.01590 \\ 0.01495 \\ 0.01382 \\ 0.06891 \\ 0.07791 \\ 0.08373 \\ 0.08694 \\ 0.02814 \\ 0.02940 \\ 0.0248 \\ 0.022951 \\ 0.05691 \\ 0.08028 \\ 0.12227 \\ 0.14390 \end{bmatrix} \rightarrow \begin{bmatrix} A_1 \\ A_2 \\ A_3 \\ A_4 \\ B_1 \\ B_2 \\ B_3 \\ B_4 \\ C_1 \\ C_2 \\ C_3 \\ C_4 \\ D_1 \\ D_2 \\ D_3 \\ D_4 \\ E_1 \\ E_2 \\ E_3 \\ E_4 \end{bmatrix} \quad (29)$$

The comprehensive impact weight of each factor on the evaluation index is calculated using eq. (29), as shown in tab. 7. It can be deduced that the order of the effect of each factor on the evaluation index is E > C > D > A > B. Moreover, by comparing the weights of each level for each factor, it can be seen that at different levels of the five factors, the levels that have the greatest impact weight on the results are A_2, B_1, C_4, D_4, and E_4. Therefore, the optimal solution obtained using the weight matrix method while considering evaluation indexes I and II is $A_2B_1C_4D_4E_4$ (Define it as solution 19).

Table 7. Analysis results obtained from the weight matrix

Factors	A	B	C	D	E
Weights	0.10401	0.06060	0.31749	0.11453	0.40336
Weight order	E > C > D > A > B				
Superior levels	A_2	B_1	C_4	D_4	E_4
Optimal scheme	$A_2B_1C_4D_4E_4$				

Figure 7. Comparison of optimal solutions

In order to verify the performance advantages of the optimal solution obtained using the weight matrix method, the evaluation index values obtained from the three optimal solutions are compared with those of the 16 groups of orthogonal test solutions, as shown in fig. 7. It can be observed from fig. 7 that in the same case, the lowest T_{ave} is obtained in solution 7, while T_{ave} in solution 17 is only 0.32 °C higher than that in solution 7. However, its ΔP is 1.87 kPa lower than that in solution 7. Therefore, solution 17 is superior when only T_{ave} is considered. Similarly, when only considering ΔP, solution 18 has the lo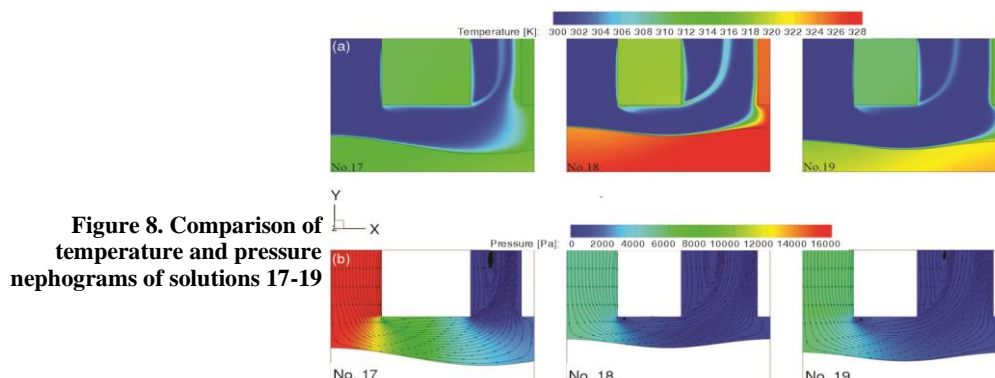west ΔP while its T_{ave} is relatively high. Solution 19 is obtained by comprehensively considering the temperature and pressure drop. Its T_{ave} is 6.89 °C lower than that in solution 18, and its ΔP is 10.27 kPa lower than that in solution 17. Figure 8 shows the comparison of temperature and pressure nephograms, and it can be seen that solution 19 has moderate T_{ave} and ΔP.

To further demonstrate the performance advantages of the optimized solutions, the performance evaluation criteria (PEC) for solutions 17-19 are compared using the conventional MMC as a benchmark. The PEC is expressed as:

$$PEC = \frac{\dfrac{Nu}{Nu_0}}{\left(\dfrac{f}{f_0}\right)^{1/3}} \tag{30}$$

where Nu_0 and f_0 represent the Nusselt number and friction factor of MMC, respectively. The comparison results are shown in tab. 8. It can be seen that the PEC of the three optimized solutions is higher than that of MMC. It is worth noting that optimized solution 19 achieved the highest PEC, which increased by 67.5% compared to MMC. Therefore, The solution 19 obtained using the weight matrix analysis method has the optimal comprehensive heat transfer performance.

Comparison of two-phase boiling flow and heat transfer characteristics of MMC and CB-MMC.

The subcooled boiling flow and heat transfer characteristics of MMC and CB-MMC in two-phase are numerically studied in this section. They both adopt the geometrical parameters of the optimal solution 19 ($A_2B_1C_4D_4E_4$). The boundary conditions are as: the channel mass flow rate is set at 1100 kg/m²s and the boiling coolant enters the heat sink at 59 °C. The heat flux of 200 W/cm², 300 W/cm², and 400 W/cm² are set at the bottom of the heat sink. The thermophysical properties of the HFE-7100 during boiling are shown in tab. 2.

1832

Cheng, J., *et al.*: Study on Single-Phase and Two-Phase Flow and …
THERMAL SCIENCE: Year 2024, Vol. 28, No. 2C, pp. 1819-1836

Figure 8. Comparison of temperature and pressure nephograms of solutions 17-19

Table 8. Comparison of PEC

Solutions	MMC	17	18	19
Nu	4.435	4.429	3.519	3.921
f	0.927	0.664	0.266	0.145
PEC	1	1.139	1.227	1.675

Figure 9 shows the variation of the T_{ave} and ΔP of MMC and optimized CB-MMC under subcooled flow boiling for three heat flux conditions. Figures 9(a) and 9(b) shows that T_{ave} first rapidly increases with time, and then tends to be basically stable at almost 15 ms with a slight fluctuation. When the heat flux increases, the T_{ave} values in MMC and CB-MMC equally increase. In contrast to the single-phase flow and heat transfer characteristics presented in the previous study, the T_{ave} values of MMC and CB-MMC are basically the same. It can be observed from figs. 9(c) and 9(d) that ΔP increases with time and reaches dynamic fluctuation equilibrium at almost 10 ms. It then oscillates at a specific value. This is basically consistent with the results of Luo *et al.* [40]. Moreover, it is shown that the average values of ΔP fluctuation increase with the heat flux increasing, and the fluctuation amplitudes become larger. However, CB-MMC shows a more stable fluctuation trend of ΔP compared with MMC.
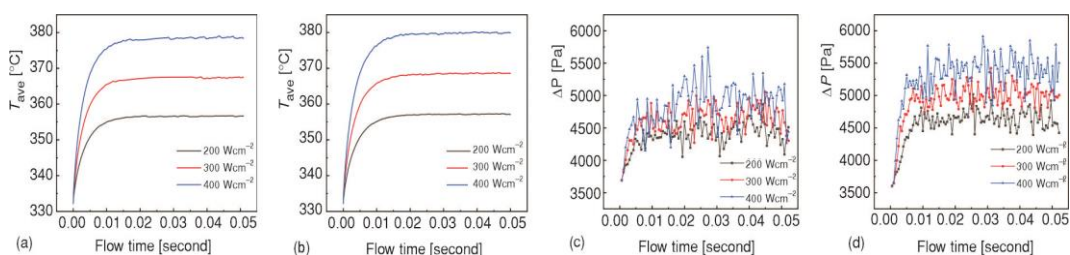

Figure 9. The change of T_{ave} (a) MMC and (b) CB-MMC and ΔP (c) MMC and (d) CB-MMC under subcooled flow boiling
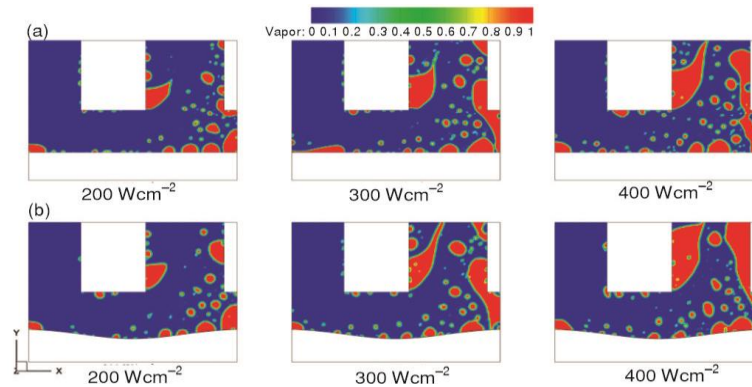
Figures 10 and 11 show the generation, growth, and movement of bubbles in MMC and CB-MMC. More precisely, fig. 10 illustrates the variation of the vapor phase nephograms in MMC and CB-MMC with flow time for the heat flux of 400 W/cm^2. It can be seen that at 0.002 seconds, the bubbles are first generated at the bottom of the channel, and the isolated bubbles are mainly concentrated near the downstream outlet. This can be considered as the starting point of nuclear boiling [41]. Due to the hydrophilicity of HFE-7100, the bubbles quickly separate the channel wall after nucleation and flow out of the microchannel. The periodic generation and outflow of bubbles cause the pressure fluctuation in the channel, as shown

in fig. 9(c) and 9(d). At this time, the phase transition only locally occurs, and the heat taken away by small bubbles is limited. Thus, the temperature of MMC and CB-MMC continues to increase, as shown in figs. 9(a) and 9(b). With the further occurrence of boiling, more nucleation sites are activated, the bubble generation area extends to the whole channel bottom, and more bubbles converge into large bubbles to form membrane boiling. From 0.004 seconds to 0.008 seconds, the vapor region changes from nuclear boiling to membrane boiling. From 0.008 seconds to 0.010 seconds, the volume fraction of vapor in the channel is basically unchanged and the boiling reaches a steady state. Afterwards, nuclear boiling and local membrane boiling alternately occur, and then exit the channel. This dynamic behavior of bubbles results in pressure fluctuations after boiling stabilization. In addition, the periodic removal of heat by bubbles causes T_{ave} to fluctuate in a similar way to the pressure drop. This is consistent with the results obtained by Pan *et al.* [24]. By comparing the vapor phase nephograms of MMC and CB-MMC, it can be deduced that when the boiling reaches a stable state, more bubbles are generated in the CB-MMC to ensure sufficient heat exchange, thus showing more stable temperature fluctuations.
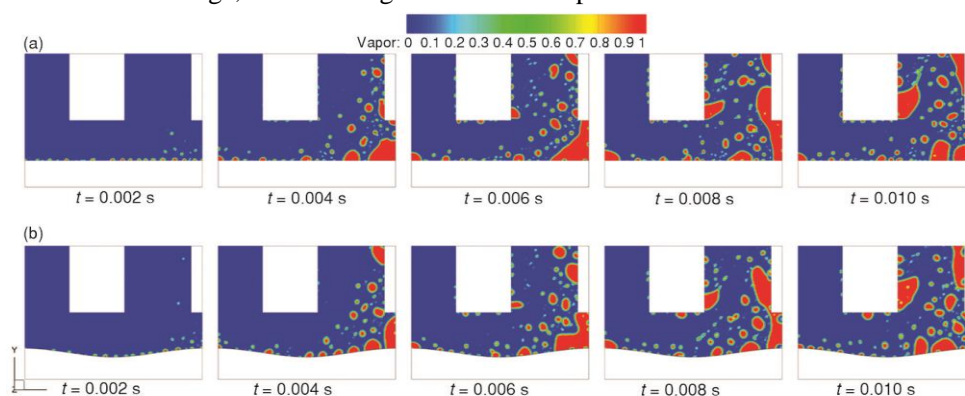
Figure 10. The changes in vapor phase nephograms of;
(a) MMC and (b) CB-MMC at 400 W/cm²

  Figure 11 shows a comparison between the vapor phase nephograms of MMC and CB-MMC under different heat fluxes at a fixed time. It can be seen that when the heat flux increases, the proportions of vapor phase in the channel increase, and thus the ΔP values of MMC and CB-MMC both increase, fig. 9(c) and 9(d). Moreover, the addition of corrugated bottom increases the area of bubble nucleation at the bottom, which leads to more bubbles, thus taking more heat away. More nucleation points result in more bubbles growing, gathering, and discharging, which results in a higher pressure drop in the CB-MMC. As mentioned in cection *Comparison of single-phase flow and heat transfer characteristics of MMC and CB-MMC*, the corrugated bottom surface and the inlet and outlet channels in CB-MMC are connected into the U-shaped channel, which slows down the reduction of the flow velocity after the coolant enters the microchannel, and thus the bubbles in CB-MMC are more likely to regularly converge into large bubbles. Therefore, CB-MMC in fig. 9(d) has a more uniform pressure fluctuation. In addition, it can be deduced that when the heat flux increases, a strip-shaped drying area starts to appear on the left side wall of the outlet manifold. This is because the fluid forms vortex at the outlet of the manifold, where bubbles gather and grow, while the low flow velocity near the outlet cannot discharge the bubbles in time, which results in the generation of large strip-shaped bubbles [32].

1834

Cheng, J., *et al.*: Study on Single-Phase and Two-Phase Flow and …
THERMAL SCIENCE: Year 2024, Vol. 28, No. 2C, pp. 1819-1836

Figure 11. Comparison between the vapor phase nephograms of;
(a) MMC and (b) CB-MMC at 0.025 seconds

Conclusions

The flow and heat transfer characteristics of HFE-7100 in MMC and CB-MMC are numerically studied under the single-phase and two-phase flow conditions. The main conclusions are as follows.

- In the single-phase flow of HFE-7100, in MMC and CB-MMC, the Tave values decrease with the flow rate increasing, while the ΔP values show an increasing trend. When the channel mass-flow rate of 1500 kg/m^{2}s, the CB-MMC reduces the pressure drop by 4.1% at a temperature reduction of less than 1% compared to the MMC. Under the same conditions, CB-MMC shows lower T_{ave} and ΔP. At both T_{ave} of 48 °C, the pressure drop of the MMC increases by 9.3% compared to the CB-MMC. Thus the CB-MMC has higher flow and convective heat transfer performance than MMC in single-phase flow.
- A multi-factor analysis of the structural parameters in CB-MMC is performed using the orthogonal test method to obtain optimal solutions 17-19, respectively. By comparison, it is found that solution 19, obtained using the weight matrix analysis method, obtained a more suitable comprehensive heat transfer performance with a T_{ave} 6.89 °C lower than that in solution 18 and a ΔP 10.27 kPa lower than that in solution 17. It is also found that the PEC of all three optimal solutions is higher than that of the MMC. The optimal solution 19 has the highest PEC with an increase of 67.5% compared to the MMC.
- When subcooled boiling of HFE-7100 occurs in the microchannel, the speeds of bubbles growing, gathering, and discharging increase, and thus the magnitude of the fluctuations of ΔP increases with the increase of the heat flux, which also leads to small fluctuations of T_{ave} after boiling equilibrium is reached. It can be deduced that the vapor bubbles in CB-MMC are more easily generated and discharged by comparing the boiling bubble characteristics in MMC and CB-MMC, and the fluctuations of ΔP and T_{ave} in the microchannel are more uniform. Therefore, CB-MMC also shows higher two-phase flow and boiling heat transfer performance.

Cheng, J., *et al.*: Study on Single-Phase and Two-Phase Flow and …
THERMAL SCIENCE: Year 2024, Vol. 28, No. 2C, pp. 1819-1836

1835

Nomenclature

C_p – specific heat capacity, [Jkg^{-1}K^{-1}]
G_{in} – mass flow rate at inlet, [kgm^{-2}s^{-1}]
H_a – amplitude of single-cell model, [μm]
i_{lv} – specific enthalpy, [kJkg^{-1}]
k – thermal conductivity, [Wm^{-1}K^{-1}]
L_{in} – length of inlet, [μm]
L_{out} – length of outlet, [μm]
L_{div} – length of divider, [μm]
L_{sub} – height of substrate, [μm]
L_c – height of channel, [μm]
ΔP – pressure drop, [kPa]
R – range, [–]
T_{ave} – average temperature, [K]
W_f – width of fin, [μm]
W_c – width of channel, [μm]

Greek symbols

α – volume fraction, [–]

$\dot{\alpha}_{lv}$ – liquid fraction generation rate, [s^{-1}]
λ – wavelength of single-cell model, [μm]
μ – dynamic viscosity, [kgm^{-1}s^{-1}]
ρ – density, [kgm^{-3}]
σ – surface tension coefficient, [Nm^{-1}]
$\dot{v}_{lv}$ – volumetric evaporation rate, [s^{-1}]
ω – weight matrix, [–]

Subscripts

l – liquid phase, [–]
lv – liquid-vapor phase change, [–]
s – solid, [–]
sat – saturation state, [–]
v – vapor phase, [–]
I – evaluation indexes I, [–]
II – evaluation indexes II, [–]

References

[1] Ebadian, M. A., Lin, C. X., A Review of High-Heat-Flux Heat Removal Technologies, *Journal of Heat Transfer*, *133* (2011), 11, pp. 1-11
[2] Tuckerman, D. B., Pease, R. F. W., High-Performance Heat Sinking for VLSI, *IEEE Electron Device Letters*, *2* (1981), 5, pp. 126-129
[3] Ye, M., *et al.*, Experimental Study on Heat Transfer Performance and Flow Visualization in Microchannels with Micropillars, *Thermal Science, 26* (2022), 5B, pp. 4169-4178
[4] Bashir, S., *et al.*, Simulations of Convective Heat Transfer in Rectangular Microchannel Using Thermal Lattice Boltzmann Method, *Thermal Science, 26* (2022), Special Issue 1, pp. 219-228
[5] Vinoth, R., Senthil, K., Numerical Study of Inlet Cross-Section Effect on Oblique Finned Microchannel Heat Sink, *Thermal Science, 22* (2018), 6B, pp. 2747-2757
[6] Gunnasegaran, P., *et al.*, The Effect of Geometrical Parameters on Heat Transfer Characteristics of Microchannels Heat Sink with Different Shapes, *International Communications in Heat and Mass Transfer*, *37* (2010), 8, pp. 1078-1086
[7] Kose, H. A., *et al.*, Parametric Study and Optimization of Microchannel Heat Sinks with Various Shapes, *Applied Thermal Engineering*, *211* (2022), 118368
[8] Peng, X. F., Peterson, G. P., Convective Heat Transfer and Flow Friction for Water Flow in Microchannel Structures, *International Journal of Heat and Mass Transfer*, *39* (1996), 12, pp. 2599-2608
[9] Anwar, M., *et al.*, Numerical Study for Heat Transfer Enhancement Using Cuo Water Nanofluids Through Mini-Channel Heat Sinks for Microprocessor Cooling, *Thermal Science*, *24* (2020), 5A, pp. 2965-2976
[10] Sahar, A. M., *et al.*, Effect of Hydraulic Diameter and Aspect Ratio on Single Phase Flow and Heat Transfer in a Rectangular Microchannel, *Applied Thermal Engineering*, *115* (2017), Mar., pp. 793-814
[11] Yuan, B., *et al.*, Heat Transfer Enhancement on Micro-Pin-Finned Surfaces Under High-Frequency Reciprocating Flow, *Applied Thermal Engineering*, *175* (2020), 115378
[12] Esmaili, Q., *et al.*, Experimental Analysis of Heat Transfer in Ribbed Microchannel, *International Journal of Thermal Sciences*, *130* (2018), Aug., pp. 140-147
[13] Feng, S., *et al.*, Thermal Management of 3D Chip with Non-Uniform Hotspots by Integrated Gradient Distribution Annular-Cavity Micro-Pin Fins, *Applied Thermal Engineering*, *182* (2021), 116132
[14] Wan, Z., *et al.*, Flow Characteristics and Heat Transfer Performance of Half-Corrugated Microchannels, *Applied Thermal Engineering*, *123* (2017), Aug., pp. 1140-1151
[15] Kermani, E., *et al.*, Experimental Investigation of Heat Transfer Performance of a Manifold Microchannel Heat Sink for Cooling of Concentrated Solar Cells, *Proceedings*, 59th Electronic Components and Technology Conference, San Diego, Cal., USA, 2009, pp. 453-459
[16] Harpole, G. M., Eninger, J. E., Microchannel Heat-Exchanger Optimization, *Proceedings*, 7th Annual IEEE Semiconductor Thermal Measurement and Manag. Sym., Scottsdale, Ariz., USA, 1991, pp. 59-63

[17] Chen, C., *et al*., Investigation of Flow and Heat Transfer Performance of the Manifold Microchannel with Different Manifold Arrangements, *Case Studies in Thermal Engineering*, *34* (2022), 102073

[18] Tang, W., *et al*., Improvement of Flow Distribution and Heat Transfer Performance of a Self-Similarity Heat Sink with a Modification to Its Structure, *Applied Thermal Eng.*, *121* (2017), July, pp. 163-171

[19] Ju, X., *et al*., Numerical Investigation of a Novel Manifold Micro-Pin-Fin Heat Sink Combining Chessboard Nozzle-Jet Concept for Ultra-High Heat Flux Removal, *International Journal of Heat and Mass Transfer*, *126* (2018), Part B, pp. 1206-1218

[20] Pourfattah, F., *et al*., On the Thermal Characteristics of a Manifold Microchannel Heat Sink Subjected to Nanofluid Using Two-Phase Flow Simulation, *International Journal of Heat and Mass Transfer*, *143* (2019), 118518

[21] Pan, Y. H., *et al*., Study on the Effect of Varying Channel Aspect Ratio on Heat Transfer Performance of Manifold Microchannel Heat Sink, *International Journal of Heat and Mass Transfer*, *163* (2020), 120461

[22] Huang, X., *et al*., Heat Transfer Enhancement on a Microchannel Heat Sink with Impinging Jets and Dimples, *International Journal of Heat and Mass Transfer*, *112* (2017), Sept., pp. 113-124

[23] Adio, S. A., *et al*., Thermal and Entropy Analysis of a Manifold Microchannel Heat Sink Operating on CuO-Water Nanofluid, *J. of the Brazilian Society of Mech. Sciences and Eng.*, *43* (2021), 2, pp. 1-15

[24] Pan, Y. H., *et al*., Study on the Flow and Heat Transfer Characteristics of Pin-Fin Manifold Microchannel Heat Sink, *International Journal of Heat and Mass Transfer*, *183* (2022), 122052

[25] Pan, Y. H., *et al*., Numerical Study on Heat Transfer Characteristics of a Pin–Fin Staggered Manifold Microchannel Heat Sink, *Applied Thermal Engineering*, *219* (2023), 119436

[26] Chen, C., *et al*., Improvement of Flow and Heat Transfer Performance of Manifold Microchannel with Porous Fins, *Applied Thermal Engineering*, *206* (2022), 118129

[27] Karayiannis, T. G., Mahmoud, M. M., Flow Boiling in Microchannels: Fundamentals and Applications, *Applied Thermal Engineering*, *115* (2017), Mar., pp. 1372-1397

[28] Drummond, K. P., *et al*., A Hierarchical Manifold Microchannel Heat Sink Array for High-Heat-Flux Two-Phase Cooling of Electronics, *Int. J. of Heat and Mass Transfer*, *117* (2018), Feb., pp. 319-330

[29] Xie, W., *et al*., Numerical Investigation of Flow Boiling in Manifold Microchannel-Based Heat Exchangers, *International Journal of Heat and Mass Transfer*, *163* (2020), 120493

[30] Mukherjee, A., Kandlikar, S. G., Numerical Simulation of Growth of a Vapor Bubble During Flow Boiling of Water in a Microchannel, *Microfluidics and Nanofluidics*, *1* (2005), 2, pp. 137-145

[31] Lin, Y., *et al*., Single-Phase and Two-Phase Flow and Heat Transfer in Microchannel Heat Sink with Various Manifold Arrangements, *International Journal of Heat and Mass Transfer*, *171* (2021), 121118

[32] Luo, Y., *et al*., A Numerical Study of Subcooled Flow Boiling in a Manifold Microchannel Heat Sink with Varying Inlet-to-Outlet Width Ratio, *Int. J. of Heat and Mass Transfer*, *139* (2019), Aug., pp. 554-563

[33] Akbarzadeh, M., *et al*., Influences of Corrugation Profiles on Entropy Generation, Heat Transfer, Pressure Drop, and Performance in a Wavy Channel, *Applied Thermal Engineering*, *116* (2017), Apr., pp. 278-291

[34] Lee, W. H., A Pressure Iteration Scheme for Two-Phase Flow Modeling, in: *Multiphase Transport Fundamentals ,Reactor Safety, Applications* (Ed. T.N. Veziroglu), Hemisphere Pub., Washington, 1980

[35] Yang, Z., *et al*., Numerical and Experimental Investigation of Two Phase Flow During Boiling in a Coiled Tube, *International Journal of Heat and Mass Transfer*, *51* (2008), 5-6, pp. 1003-1016

[36] Chen, B., *et al*., Flooded Two-Phase Flow Dynamics and Heat Transfer With Engineered Wettability on Microstructured Surfaces, *Journal of Heat Transfer*, *137* (2015), 9, 091021

[37] Peng, M., *et al*., Numerical Study on Flow and Heat Transfer in a Multi-Jet Microchannel Heat Sink, *International Journal of Heat and Mass Transfer*, *157* (2020), 119982

[38] Zuo, W., *et al*., Orthogonal Experimental Design and Fuzzy Grey Relational Analysis for Emitter Efficiency of the Micro-Cylindrical Combustor with a Step, *App. Ther. Eng.*, *103* (2016), June, pp. 945-951

[39] E, J. Q., *et al*., Orthogonal Experimental Design of Liquid-Cooling Structure on the Cooling Effect of a Liquid-Cooled Battery Thermal Management System, *App. Ther. Eng.*, *132* (2018), Mar., pp. 508-520

[40] Luo, Y., *et al*., Analysis of Thermal Performance and Pressure Loss of Subcooled Flow Boiling in Manifold Microchannel Heat Sink, *International Journal of Heat and Mass Transfer*, *162* (2020), 120362

[41] Yuan, Y., *et al*., Numerical Investigation of Flow Boiling Heat Transfer in Manifold Microchannels, *Applied Thermal Engineering*, *217* (2022), 119268